Princeton Plasma Physics Laboratory

PPPL-5361

NSTX-U L-mode plasmas in support of transport and turbulence validation

W. Guttenfelder, S.M. Kaye, R.E. Bell, A. Diallo, B.P. LeBlanc, and M. Podestà

February 2017

Prepared for the U.S. Department of Energy under Contract DE-AC02-09CH11466.

Princeton Plasma Physics Laboratory
Report Disclaimers

Full Legal Disclaimer

Trademark Disclaimer

PPPL Report Availability

Princeton Plasma Physics Laboratory:

http://www.pppl.gov/techreports.cfm

Office of Scientific and Technical Information (OSTI):

http://www.osti.gov/scitech/

Related Links:

U.S. Department of Energy

U.S. Department of Energy Office of Science

U.S. Department of Energy Office of Fusion Energy Sciences

NSTX-U L-mode plasmas in support of transport and turbulence validation

W. Guttenfelder[1*], S.M. Kaye[1], D.M. Kriete[2], R.E. Bell[1], A. Diallo[1], B.P. LeBlanc[1], M. Podesta[1], S.A. Sabbagh[3], D. Smith[2]

[1] *Princeton Plasma Physics Laboratory, Princeton NJ 08543*
[2]*University of Wisconsin-Madison, Madison, WI 53706*
[3]*Columbia University, New York, NY 10027*

* e-mail: wgutten@pppl.gov

Abstract

A variety of stationary L-mode plasmas were successfully developed during the first run campaign of the National Spherical Torus Experiment – Upgrade (NSTX-U) project to support numerous core, edge and boundary research activities. The NSTX-U L-mode discharges span a range of plasma current, I_p=0.65-1.0 MA, and line-averaged density, $\langle n_e \rangle$=1-4×10^{19} m^{-3}, using a magnetic field B_T=0.63 T larger than previous NSTX operational limits (≤0.55 T). The higher density L-modes were sustained with up to 3 MW of neutral beam heating. Transport analysis shows that ion thermal transport approaches neoclassical levels at the relatively high collisionalities required to avoid transition to H-mode. Ion-scale turbulence measurements from 2D beam emission spectroscopy (BES) show significant fluctuation amplitudes. Initial gyrokinetic analysis predicts that ion temperature gradient (ITG) modes are unstable around normalized radii ρ=0.6-0.7, although E×B shearing rates are larger than the linear growth rates over much of that region. The electron temperature gradient (ETG) instability at electron scales is also found unstable and nonlinear ETG simulations predict significant electron thermal transport outside ρ>0.5. Deeper in the core (ρ<0.6) of higher beta (β_T≈4%, β_N≈2) L-modes, the electromagnetic microtearing modes are also unstable, possibly contributing to the anomalous electron thermal transport in those cases. In contrast, at lower beta (β_T≈2%, β_N≈1), the microtearing modes are very weak and almost completely stabilized. These low aspect ratio, modest beta discharges (R/a~1.6, β_N~1-2) provide an experimental target for validation and cross-code benchmarking that is intermediate between high aspect ratio, low beta (R/a ~ 3, β_N ~ 1-2) where the bulk of gyrokinetic validation studies exist, and low aspect ratio, high beta (R/a ~ 1.6, β_N ~ 5) where gyrokinetic simulations are less tested and challenged by stronger electromagnetic, equilibrium, and non-local effects (at large $\rho_* = \rho_i/a$).

I. Introduction

A key priority for transport research in low aspect ratio (R/a<2) spherical tokamaks (STs) is to understand transport and confinement scaling in high-performance, high beta plasmas. In particular, the favorable collisionality scaling, $B\tau_E \sim \nu_*^{-1}$, observed previously in NSTX [1-3] and MAST [4,5] H-modes has significant implications on the required machine size and heating power at low collisionality conditions envisioned for a future possible Component Test Facility [6-8], Fusion Nuclear Science Facility [9,10], or Pilot Plant [11,12]. As ion thermal transport tends to be close to neoclassical theory in NSTX and MAST H-modes, understanding the cause of anomalous electron thermal transport is of primary importance.

Previous core transport validation efforts have focused on high-beta NSTX H-mode plasmas where microtearing mode (MTM) [13-15] or kinetic ballooning mode (KBM) [16] instabilities are predicted to be unstable. These modes are fundamentally electromagnetic, only becoming unstable above a threshold in plasma beta, and are distinct from the electrostatic ion temperature gradient (ITG) and trapped electron mode (TEM) instabilities that are typically expected to determine confinement at conventional aspect ratio (R/a~3). Nonlinear gyrokinetic simulations predict significant transport from MTM [13,17] and KBM [16,18-23] that is very sensitive to beta due to coupling to magnetic fluctuations. However, demonstrating sufficiently resolved, saturated turbulence simulations at high beta is especially challenging due to stringent numerical resolution requirements.

In addition, the previous electromagnetic simulations based on NSTX high-beta H-modes were run in the local limit, meaning $\rho_* = \rho_i/a$ is assumed to be sufficiently small ($\rho_* \rightarrow 0$) so that equilibrium and plasma gradient information is only used at a single radial location. However, the local stability characteristics are predicted to change with radius as the driving gradients and equilibrium properties vary. The strength of the growth rate, and the strength of the E×B shearing which can suppress turbulence [24-27], vary over a region that is relatively narrow in terms of ion gyroradii, ~20-30 ρ_i [16], due to the larger values of $\rho_* \sim 1/B$ in STs. It could therefore be expected that quantitative predictions of transport will change in global/non-local simulations that account for profile variations. Furthermore, different instabilities can be unstable simultaneously, and global electromagnetic simulations will likely be required to determine what mode dominates or whether multiple instabilities can co-exist in the nonlinear saturated state.

Global electrostatic nonlinear simulations for NSTX L-mode plasma [28] unstable to ITG/TEM show that non-local effects (with $\rho_* \sim 1/130$) are in fact important as they smooth out strong radial variation in transport predicted from local simulations [29]. These simulations were run in the electrostatic limit as beta was sufficiently small that electromagnetic effects were not predicted to be important. However, high beta H-mode plasmas are at much larger beta and local, linear simulations

typically predict electromagnetic effects are critical to include. Therefore it is important to turn to global electromagnetic simulations.

A number of recent papers have begun to address global toroidal electromagnetic simulations. Linear simulations have investigated MTM stability [30,31], and more generally cross-code benchmarking exercise of the transition between ITG to KBM as beta is increased [32,33]. Global EM nonlinear simulations have been utilized in a number of core transport validation studies based on experimental data [34-36], although it would appear beta was small enough in these cases that the influence of electromagnetic effects was not noteworthy beyond their inclusion. Both linear and nonlinear global EM simulations have also been run for H-mode edge pedestal parameters [37-41] where electromagnetic effects are more critical. However, there have been no core global EM gyrokinetic simulations run for low-aspect-ratio spherical tokamak plasmas to date.

Given the complexity of the high beta H-modes cases, it is desirable to provide an intermediate validation condition that bridges high aspect ratio, low beta ($R/a \sim 3$, $\beta_N \sim 1\text{-}2$) where the bulk of gyrokinetic validation studies exist, and low aspect ratio, high beta ($R/a \sim 1.5$, $\beta_N \sim 5$) where GK simulations are less tested and challenged by stronger electromagnetic, equilibrium, and non-local effects (at large $\rho_* = \rho_i/a$). To provide such an experimental "intermediate" target for validation and cross-code benchmarking, a variety of stationary L-mode plasmas were successfully developed in the National Spherical Torus Experiment – Upgrade (NSTX-U) [42,43] during the recently completed first run campaign [44]. Normalized beta values between β_N~1-2 (R/a~1.6) were achieved for 0.5-1 second flat-top, providing a useful target for the intermediate validation condition.

The remainder of the paper is organized as follows. Characteristics of the NSTX-U L-mode discharges are presented in Sec. II including time-history, characteristic equilibria and kinetic profiles, as well as observed MHD behavior. Transport analysis is presented in Sec. III, illustrating that ion thermal transport is well-described by neoclassical theory due to the relatively large collisionality in these L-modes. Sec. IV shows characteristics of the large amplitude, broadband, ion-scale fluctuations measured by the Beam Emission Spectroscopy diagnostic. Initial linear and nonlinear local gyrokinetic simulations are given in Sec. V. Even for the lower-beta L-mode plasmas, a complex environment is predicted including electrostatic ITG and electromagnetic MTM instabilities at ion scales. There is a significant radial variation of growth rates and E×B shearing rates that suggest non-local effects will likely be important in these plasmas, providing a valuable test case of global electromagnetic gyrokinetic simulations. Nonlinear electron scale simulations indicate ETG turbulence can provide experimental heat fluxes, also suggesting multiscale effects are likely important in some regions. A discussion and summary are given in Sec. VI.

II. L-mode discharges and characteristics

During NSTX-U commissioning in 2016, run time was dedicated to establish long, steady L-mode plasmas over a range of plasma current, neutral beam injection (NBI) heating power and density to support a number of core, boundary and scrape-off layer research activities. Fig. 1 shows a number of time traces for four representative L-mode discharges that span a range of plasma current, I_p=0.65-0.8 MA, NBI heating power (P_{NBI}=1-2.6 MW), and line-averaged density $\langle n_e \rangle$=1-4×10^{19} m^{-3}. All the discharges were run with magnetic field B_T=0.63 T larger than previous NSTX operational limits (≤0.55 T). At lower plasma current (0.65 MA), plasma discharges were successful run out to >2.0 seconds with a flat-top of >1.0 sec. Upgrades to the plasma control system (PCS) and real time EFIT also allowed for slow I_p ramp-down to avoid disruptions. The slow I_p ramp-down was not always utilized, as it requires additional ohmic flux that could instead be used to extend the flat-top time. Additional discharges demonstrated steady L-mode operation up to I_p=1.0 MA (q95=3.7) for >0.5 sec I_p flat-top, limited only by the available ohmic flux.

Traditionally it is challenging to prevent NSTX plasmas from transitioning into H-mode with NBI heating, especially in diverted plasmas as pursued here. To avoid L-H transition over a range of NBI heating power, high field side (HFS) gas puffing was used to raise the plasma density. With sufficiently strong HFS gas puffing (seen by the rapid increase in D_α near the center stack at ~0.3 sec, shortly after the plasmas divert at ~0.23 sec) L-modes with up to ~3 MW could be sustained. NBI heating powers over P_{NBI}>4 MW were also tested but all discharges eventually transitioned into H-mode and disrupted. For the higher density (~4×10^{19} m^{-3}), higher power discharges (2.5-3 MW), normalized beta values, $\beta_N=\beta_T/(I/aB_T)\geq 2$ are achieved, as determined from EFIT equilibrium reconstructions [45,46] constrained by external magnetics (no MSE measurements were available).

All NBI-heated L-mode discharges in this paper begin to exhibit sawteeth after ~0.4 sec, observable in the neutron rate in Fig. 1, hard and soft x-rays (not shown), and electron temperature profiles (shown below). The onset of sawteeth is consistent with the occurrence of q_{min}<1 as calculated by EFIT. The sawtooth period is Δt_{ST}~25-35 ms depending on plasma density and which NBI heating source is used (at differing tangency radii).

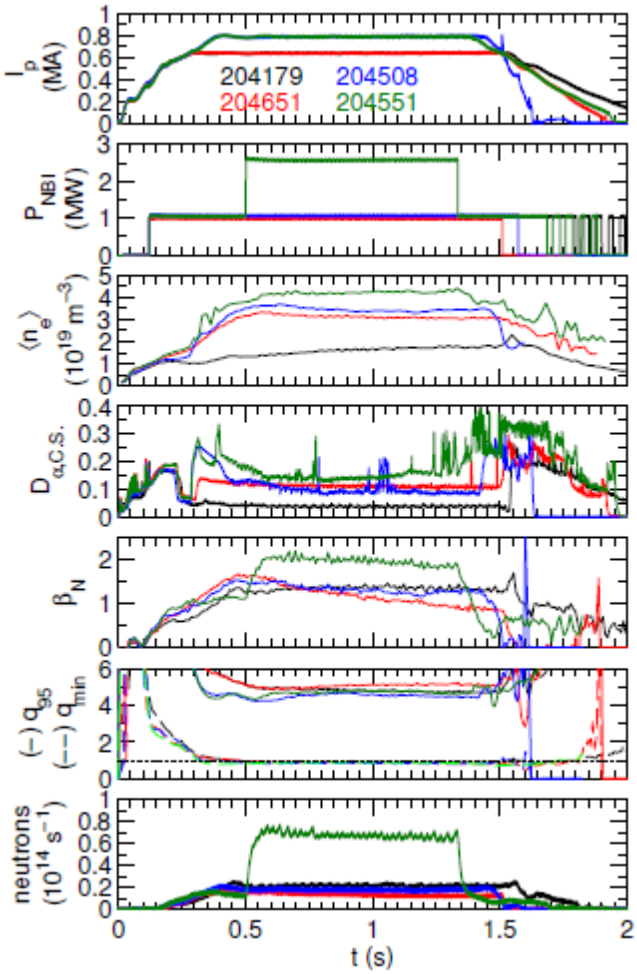

Fig.1 Time traces of plasma current, NBI power, line-averaged density, D_α measured from chord with line-of-sight near the centerstack, normalized beta, q95 and q0, and neutron rate for four NSTX-U L-mode discharges.

Table 1 provides a number of time-averaged parameters over a 200-300 ms window during the relatively stationary period of a number of L-mode discharges. For the discharges investigated in this paper the original three neutral beam sources were utilized [42] with tangency radii smaller than the magnetic axis (R_{tan}≈50, 60, 70 cm), as indicated next to the NBI power in Table 1. The normalized electron collisionality is $\nu_{*e}=(\nu^{e/i}/\varepsilon)/(\varepsilon^{1/2}\cdot v_{Te}/qR)$, and inverse normalized gyroradius, $1/\rho_{*s}=a/\rho_s$ where $\rho_s=(T_e/m_D)^{1/2}/B_T$. Both ν_{*e} and ρ_{*s} are evaluated at ρ=0.65, where ρ is a flux-surface coordinate defined using the square root of normalized toroidal flux.

Shot	Time (s)	B_T (T)	I_p (MA)	P_{NBI} (MW)	R_{tan} (cm)	n_e (10^{19} m^{-3})	W_{MHD} (kJ)	q_{95}	β_N	β_T (%)	ν_{*e} (ρ=0.65)	$1/\rho_{*s}$ (ρ=0.65)
204179	0.9-1.1	0.63	0.64	1.1	60	1.7	50	4.8	1.4	2.4	0.043	117
204508	0.9-1.1	0.63	0.79	1.1	60	3.4	62	4.6	1.3	2.7	0.15	143
204551	0.9-1.2	0.63	0.79	2.6	70,60	4.3	95	4.8	2.0	4.1	0.27	145
204651	0.9-1.1	0.63	0.64	1.0	50	3.1	42	5.1	1.1	1.9	0.40	172
204963	0.9-1.1	0.63	0.64	0.94	60	3.1	62	5.5	1.7	2.8	0.36	167

Table 1. Shot parameters for various NSTX-U L-mode plasmas averaged over the time interval indicated.

Fig. 2 shows contours of normalized poloidal flux, ψ_N, from an EFIT equilibrium reconstruction of discharge 204551 at 1.0 s to illustrate the surface shaping. Compared to high performance, high-beta plasmas (e.g. [47]), the equilibrium shaping is relatively conservative with elongation of κ=1.7, upper/lower triangularity δ=0.31/0.41, internal inductance ℓ_i=1.3, and aspect ratio R/a=0.93 m/0.59 m=1.58. The equilibrium are close to balanced double null with a slight downward bias, drsep = -(3-4) mm and inner gap around ~3 cm. Table I also shows additional quantities determined from EFIT including stored energy, W_{MHD}, edge safety factor at ψ_N=0.95, q_{95}, normalized beta, β_N, and toroidal beta, β_T.

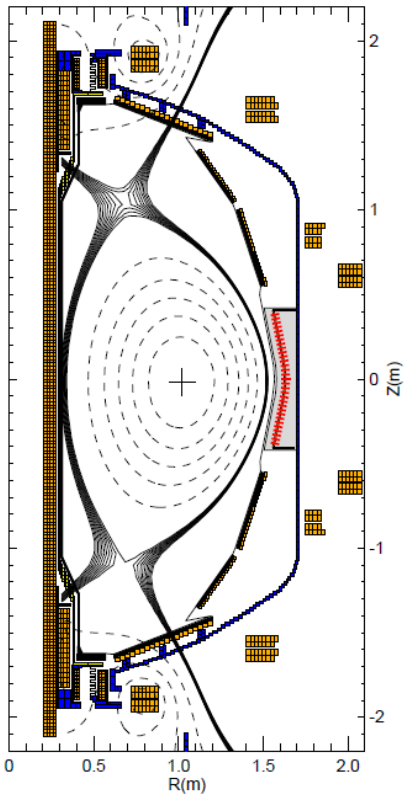

Fig. 2. EFIT equilibrium reconstruction of NSTX-U 204551.

Fig. 3 shows example plasma profiles at three time slices of discharge 204551, including electron density and temperature measured by Thomson scattering [48], and carbon temperature, density and toroidal rotation profiles measured by Charge Exchange Recombination spectroscopy [49]. The inferred deuterium density is also shown assuming fully stripped carbon and no other impurity ions ($n_D+6\cdot n_C=n_e$). Because of the relatively low carbon impurity content in these plasmas, $Z_{eff}\leq 1.4$, we choose to focus on the higher density, higher power discharge as the CHERS signals are largest and provide the lowest uncertainty in the ion temperature profiles.

The influence of the sawteeth is clearly apparent in the T_e profiles with an inversion radius around R_{inv}=125 cm. The inversion radius aligns well with the q=1 surface from the EFIT reconstructions ($\psi_{N,inv}\approx 0.27$) shown by the shaded blue region, which is an important validation since motional Stark effect measurements were unavailable to verify the internal magnetic pitch angle. The electron density profile is relatively flat inside the sawtooth inversion radius, as is the toroidal rotation profile.

Somewhat striking is that the edge rotation (R>142 cm, $\psi_N>0.8$) appears to be locked (~0 km/s). The edge rotation does unlock in discharges that transition into H-mode (with sufficient beam power). There is also evidence of unlocking in low power (1 MW) L-modes when the neutral beam source is changed to one of the new sources at larger tangency radii (Rtan=110, 120,130 cm), where the deposited torque is much further out [43]. When the NBI source is transitioned at 500 ms from Rtan=60 $\rightarrow$120 cm, an n=1 mode appears to grow from ~0 kHz on the Mirnov spectra. Based on the EFIT q-profile, the q=2 surface is $R_{q=2}\approx 144$ cm, so we speculate that the rotation is locked due to a locked 2/1 mode. Rotation profiles are unavailable to confirm the edge rotation due to the contamination of the CHERS background measurements during the use of the new NBI sources.

As a consequence of the flat core rotation and locked edge rotation there is very strong rotation shear in the region of R=125-142 cm (ψ_N=0.27-0.73 or ρ=0.37-0.68), which has consequences on the predicted microstability behavior discussed later.

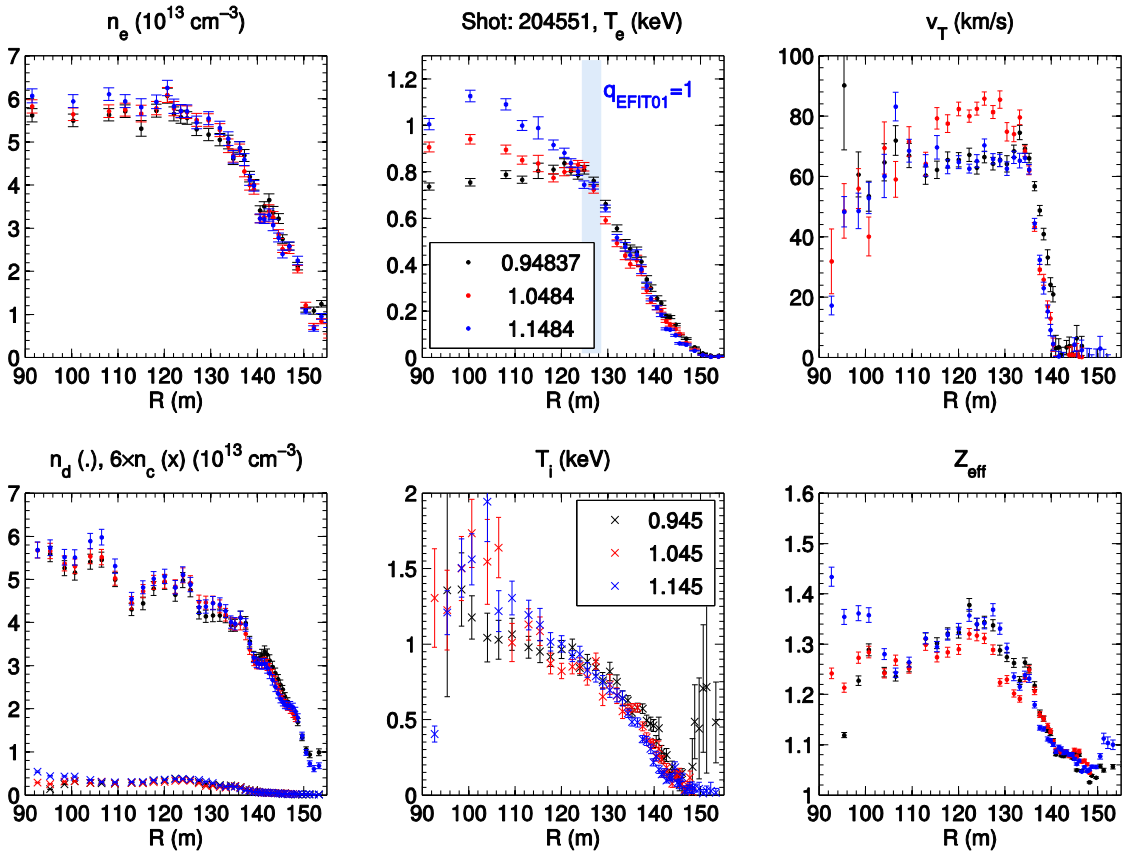

Fig. 3. Kinetic profiles of electron density and temperature, ion temperature, deuterium and carbon density, toroidal rotation velocity, and Z_{eff} at three time slices in NSTX-U 204551.

A Mirnov spectrogram of discharge 204551 is shown in Fig. 4a. The influence of the sawteeth is apparent as spikes at multiple harmonics (n=1-4). There also appears to be an n=3 mode which could be evidence of a weak 4/3 tearing mode. There is some indication of a slight flattening in the T_e profile around R=134 cm which would be consistent with this. Towards the end of the discharge (~1.35 sec) a strong n=2 mode appears that is correlated with a further reduction in rotation inwards of the q=3/2 surface, indicating the presence of a 3/2 tearing mode. This 3/2 tearing mode appeared at various times in other high β_N~2 L-mode discharges such as 204516 (Fig. 4b), an otherwise similar shot to 204551. For comparison, a spectrogram for the lower β_N=1.4 L-mode 204179 is shown in Fig. 4c.

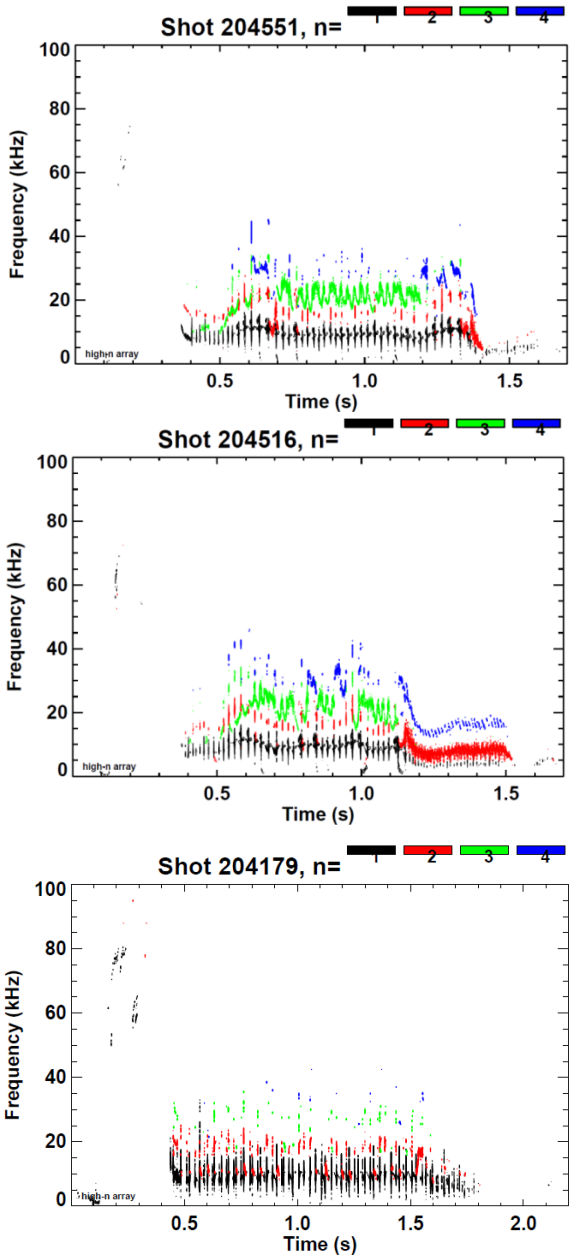

Fig. 4. Mirnov spectrograms for three NSTX-U L-modes. The different colors represent different toroidal mode numbers, n=1-4.

III. Transport analysis

Transport characteristics of the NSTX-U L-mode plasmas have been studied using the TRANSP code [50] coupled with NUBEAM [51] calculations of the neutral beam injection. As mentioned above, Z_{eff} based only on the CHERS measured carbon density is quite low in these discharges (Z_{eff}~1.2), however there is evidence from fast-ion D-alpha (FIDA) [x] and visible Brehmsstrahlung measurements that suggests $Z_{eff} \geq 2$. In the following TRANSP analysis $Z_{eff}=2$ has been assumed. Also included in the TRANSP analysis is the use of a feedback algorithm that adjusts the Anomalous Fast Ion Diffusivity

(AFID), D_{fast}, during the calculation in order to bring the calculated and measured neutron rates into agreement. It was found, especially for lower density discharges and discharges with obvious MHD activity, that up to 50% of the fast ion density/power could be lost through shine-thru, orbits leaving the main plasma and intersecting material surfaces or charge-exchange with thermal neutrals. We focus on discharges and times of interest devoid of the strong 3/2 tearing activity and the $D_{fast} \leq 4$ m^2/s in 204551. A more rigorous validation of the NUBEAM calculation against FIDA [x] and solid state neutral particle analyzer (SSNPA) [x] measurements is a necessary future task.

Results of the TRANSP analysis for 204551 over the time interval 0.9-1.2 sec are shown in Fig 5. Energy is lost predominantly through the electron channel as shown in Fig. 5c. In fact, using the experimental profiles the inferred ion heat flux is inward (negative) due to the strong collisional energy exchange and the fact that $T_i/T_e \sim 1.1$-1.2 inside $R \leq 140$ cm. A predictive TRANSP run assuming purely neoclassical ion thermal transport ($Q_i = Q_{i,nc}$) predicts $T_i \sim 90\%$ of $T_{i,exp}$ which is at the lower bound of the 1σ statistical variation (averaged over 300 ms) of the measured T_i profile shown in Fig. 5a. Predictions using Chang-Hinton [52], NCLASS [53] and NEO [54,55] give almost identical results. Changing $Z_{eff} = 2 \rightarrow 1.2$ also had little impact on the inferred transport. It is likely that ion transport in this higher density (higher collisionality) discharge is neoclassical with ~0.5 MW uncertainty in Q_i and Q_e around R=125-140 cm due to strong collisional energy coupling. There is also a ~0.5 MW statistical variation in the electron heat flux due in part to the transient behavior from the presence of sawteeth. The corresponding values of ion thermal diffusivities are around $\chi_i \approx \chi_{i,nc} \approx 1$ m^2/s over $\rho = 0.4$-0.8 (125-145 cm), where the electron thermal diffusivity increases from $\chi_e = 3$-12 m^2/s over the same region. The energy confinement times range between 30-50 ms for L-modes with comparable density spanning a total heating power (ohmic and NBI, subtracting beam losses calculated by NUBEAM) of 1.1-3.9 MW, and appear to loosely follow conventional power degradation ($\tau_E \sim P^{-2/3}$) consistent with previous non-ST L-mode results [56].

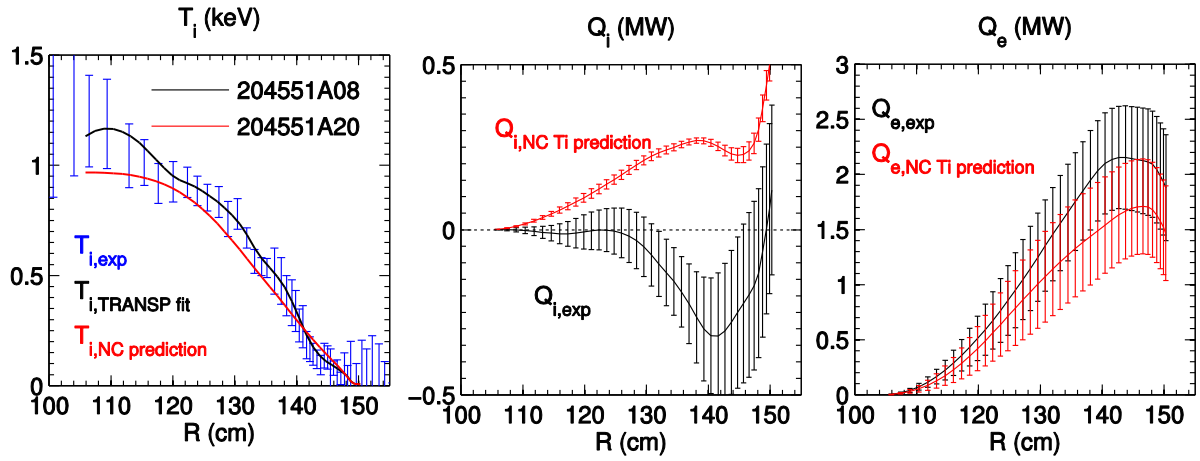

Fig. 5. (a) Ion temperature profiles, (b) ion heat fluxes, and (c) electron heat fluxes from TRANSP analysis.

IV. Turbulence measurements

Turbulence data from the University of Wisconsin 48 channel Beam Emission Spectroscopy (BES) diagnostic [57,58] was available for many of the L-mode discharges investigated. The BES channels were configured in a 2D array with spacing $\Delta R \approx 2.5$ cm, $\Delta Z \approx 3$ cm and lines-of-sight that intersect the neutral beam line between 125-150 cm (ψ_N=0.27-1.0, ρ=0.39-1.0) (Fig. 6a). Two rows of poloidally adjacent channels are used to measure cross-power, coherence and cross-phase. Fig. 6b shows that broad spectra of fluctuations are present up to 200 kHz with amplitudes increasing in radius across the six channel pairs (R=134-146 cm, ψ_N=0.57-0.90, ρ=0.58-0.85, highlighted in red in Fig. 6a). The frequency-integrated (1-200 kHz) normalized fluctuation amplitude of the normalized intensity, assumed to be proportional the normalized density fluctuations ($\delta I/I \approx 0.5 \cdot \delta n/n$ [57]) are very large ranging from ~2% at 134 cm up to 8% at 146 cm (Fig. 6c).

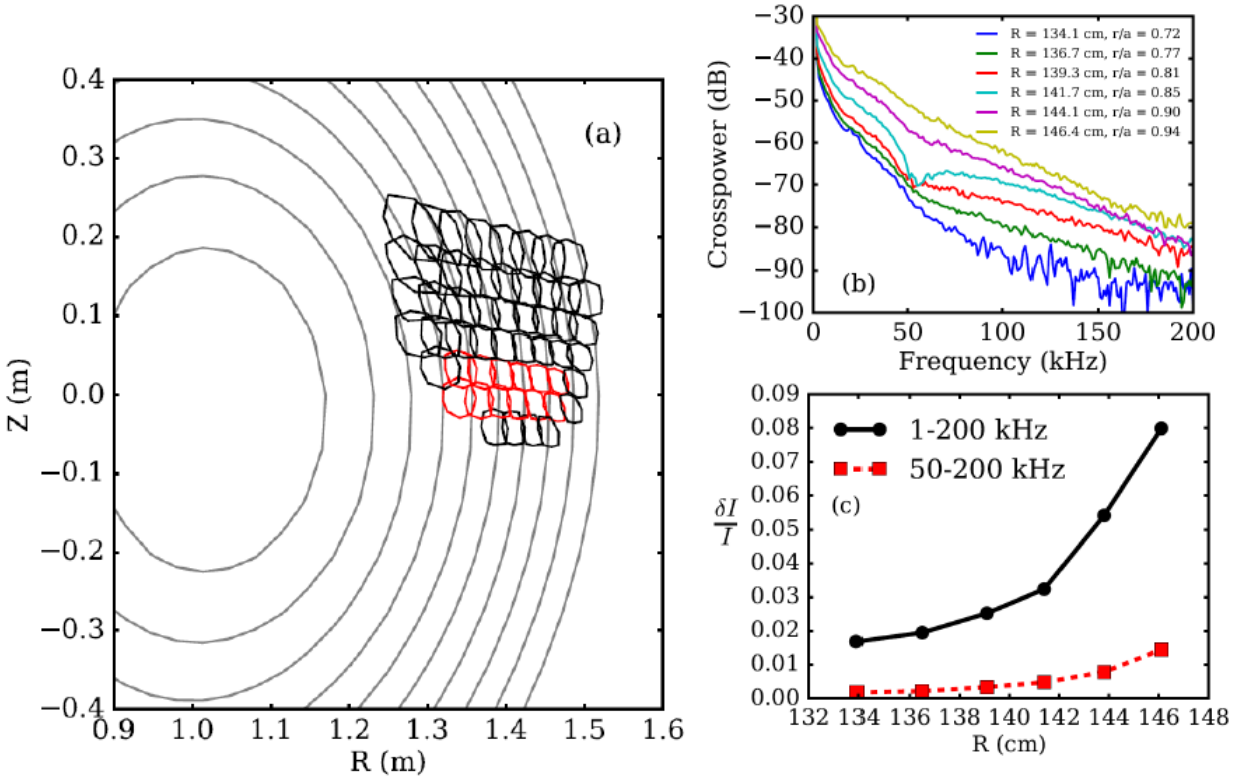

Fig. 6. (a) BES sightlines overlaid on constant-ψ_N contours from the EFIT reconstruction. Two poloidally separated rows used for cross-correlation analysis are highlighted in red. (b) Cross-power spectra at six radii using two poloidally separated rows of BES measurements. (c) Normalized fluctuation amplitude, $\delta I/I$, frequency-integrated over 1-200 kHz (solid black line) and 50-200 kHz (dashed red line).

Significant coherence is found between the poloidally adjacent channels out to 200 kHz (Fig. 7a), allowing for a meaningful cross-phase to be measured. The cross-phase provides an estimate of the

propagation direction of the fluctuations as well as the local phase velocity, $V_{ph}=\omega_{lab}/k_\theta$ where $k_\theta \approx \alpha/\Delta Z$ is the estimated local poloidal wavenumber based on the mean poloidal cross-phase.

Fig. 7b shows an example cross-phase spectra at R=139 cm (ψ_N=0.72, ρ=0.68). Interestingly, a phase velocity -13 km/s in the electron diamagnetic drift direction is found at low frequencies (<50 kHz), while an ion-directed phase velocity +11 km/s is measured at higher frequencies (50-200 kHz). The cross-coherence is above the estimate noise floor over this entire range (dashed line in Fig. 7a) giving confidence in the measured cross-phases. As a result, the spread in measured cross-phase given by the shaded region in Fig. 7b is relatively narrow so that the distinct cross-phases are statistically meaningful. Similar bi-modal cross-phases are observed at a number of radii in this L-mode plasma.

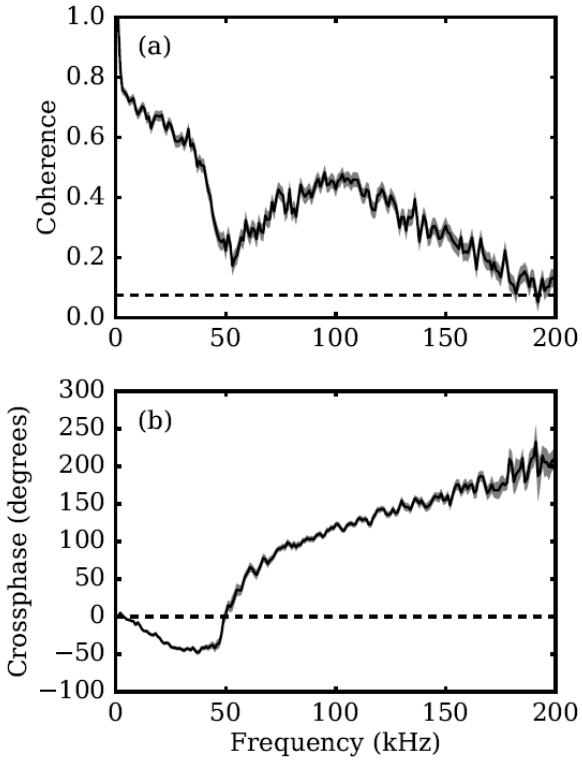

Fig. 7. (a) Coherence and (b) crossphase spectra between poloidally adjacent BES channels at R=139 cm. The dashed line in (a) gives the estimated noise floor.

Bimodal propagation suggests that two distinct turbulence mechanisms could be present in the data, and has been observed in BES measurements in other devices [60,61]. As will be discussed later, microstability analysis does in fact predict two different instabilities at ion scales in these plasmas. However, the measured frequency in the lab frame will depend on both the mode frequency in the plasma frame plus any Doppler shift due to background plasma flows, $\omega_{lab} = \omega_{mode} + \vec{k} \cdot \vec{V}_{Doppler}$. For microinstabilities the Doppler shift is due to the equilibrium $E_r \times B$ drift. NCLASS [53] calculations show

that for these L-mode discharges that $E_r = V\times B - \nabla P_i/Z_i e n_i$ is dominated by the toroidal rotation (as measured by carbon), but is reduced ~30% due to ∇P_i and the calculated neoclassical poloidal flow $V_{\theta,NC}$. For the measurements in Fig. 7 (R=139 cm), the toroidal carbon rotation is $V_{\varphi,C}$=25 km/s in the ion direction with a statistical variation of +/- 8 km/s in the interval 0.9-1.2 sec. Furthermore, as the turbulent eddies are generally expected to be aligned along the magnetic field ($k_{\|}<<k_{\perp}$), the Doppler shift projected into the poloidal plane of the BES measurements would give an apparent poloidal phase velocity $V_{\theta,C}=V_{\varphi}\cdot\tan(\alpha)$ where α is the field line angle in reference to purely toroidal [62]. The resulting Doppler shift is estimated as $V_{Doppler,\theta}$ = 9 +/- 3 km/s (in the ion direction), which implies the mode velocities the plasma frame are -4 +/- 3 km/s and +20 +/- 3 km/s. The electron mode velocity is reduced considerably while the ion velocity is increased further in the ion direction.

Additional analysis also finds that there is a very strong cross-coherence in radially separated channels for the low frequency (<50 kHz) electron-directed propagations. The cross-phases between the radially separated channels for these are near zero. The strong radial coherence and ~0 cross-phase at these low frequencies suggests that they may be due to edge shadowing, i.e. large amplitude edge fluctuations causing modulation of the neutral beam density in the core plasma where the local BES measurements are made [63]. If the low frequency fluctuations are in fact due to edge shadowing, they are not representative of the local fluctuation amplitude. If the power spectra in Fig. 6b are integrated over the higher frequency interval 50-200 kHz, much smaller local fluctuation amplitudes 0.1-1% are inferred (Fig. 6c, dashed line).

V. Gyrokinetic analysis

Linear simulations

The GYRO code [64-66] has been used to investigate linear stability properties in the region between the sawtooth inversion radius and the edge rotation locking (R~125-140 cm). The simulations below are based on NSTX-U discharge 204551 using a general representation [67] of the EFIT++ equilibrium reconstruction, kinetic electrons, kinetic deuterium and carbon ion species, collisions, and fully electromagnetic perturbations (φ, $A_{\|}$, $B_{\|}$). Linear simulations typically use 16-32 radial grid points, 12-16 energy grid points, 12 pitch angles and 14 parallel orbit mesh points (×2 signs of parallel velocity), as determined from convergence tests.

Local parameters used in the GYRO simulations are given in Table II including local safety factor (q), magnetic shear ($s=-r/q\cdot dq/dr$), ratio of electron to ion temperature, and normalized temperature and density gradients ($a/L_X=-a/X\cdot dX/dr$). The local electron beta is defined as $\beta_e=8\pi n_e T_e/B^2$ using the vacuum values of B_T=0.62 T listed in Table 1. A second set of values $\beta_{e,unit}$ are defined replacing B_T with

the quantity $B_{unit}=B_T\cdot\rho/r\cdot d\rho/dr$ [$\rho=(\Psi_t/\pi B_T)^{1/2}$, Ψ_t is the toroidal flux] as used in normalizations throughout GYRO. The parameter $\alpha_{MHD}=-q^2R_0\cdot 8\pi/B_{unit}^2\cdot dp/dr$ is a generalized MHD-α parameter [67]. The normalized electron-ion collision frequency is determined by $\nu^{e/i}=Z_{eff}\cdot\nu_{ei}$, where $\nu_{ei}=4\pi n_e e^4 \log\Lambda/(2T_e)^{3/2}m_e^{1/2}$. The E×B shear rate is given by $\gamma_E=-r/q\cdot d\omega_0/dr$ [66], where $\omega_0=-d\Phi_0/d\psi$ is the toroidal rotation frequency, Φ_0 is the equilibrium electric field potential and ψ is the poloidal flux. Frequencies are normalized to c_s/a where $c_s=(T_e/m_d)^{1/2}$.

r/a	**ψ_N**	**ρ**	**R_{out} (cm)**	**q**	**s**	**T_e/T_i**	**a/L_{Ti}**	**a/L_{Te}**	**a/L_{ne}**	**β_e (%)**	**$\beta_{e,unit}$ (%)**	**α_{MHD}**	**ν_{ei} (c_s/a)**	**γ_E (c_s/a)**
0.45	0.33	0.42	127	1.0	0.5	0.83	1.8	2.1	0.6	3.7	1.2	0.12	0.57	0.010
0.50	0.40	0.47	129	1.1	0.7	0.81	2.2	2.5	0.8	3.2	1.0	0.14	0.69	0.004
0.55	0.47	0.52	131	1.2	1.0	0.80	2.7	3.0	1.1	2.6	0.87	0.18	0.86	0.066
0.60	0.55	0.56	133	1.3	1.3	0.79	3.5	3.7	1.4	2.1	0.70	0.22	1.1	0.29
0.65	0.62	0.61	136	1.5	1.7	0.79	4.7	4.5	1.8	1.6	0.53	0.26	1.5	0.62
0.70	0.68	0.66	138	1.7	2.1	0.81	6.4	5.5	2.1	1.1	0.37	0.30	2.2	0.72
0.75	0.75	0.70	140	2.0	2.5	0.87	8.4	6.5	2.4	0.74	0.23	0.30	3.6	0.51
0.80	0.80	0.75	142	2.4	3.1	0.98	9.8	7.2	2.7	0.46	0.14	0.27	6.1	0.17

Table II: Local equilibrium and plasma parameters used in the GYRO simulations for discharge 2045551.

The linear simulations for this case predict that a broad spectra of ITG modes are unstable at ion wavenumbers ($k_\theta\rho_s<1$) outside $\rho\geq 0.61$ as expected for a lower beta L-mode discharge (Fig.8a,b). The ITG growth rates peak around $k_\theta\rho_s=0.4$ and increase in value at larger radii. As expected from the rotation profile (Fig. 3c), the E×B shearing rates at some locations are quite large and bigger than the ITG growth rates (short dashed lines in Fig. 8b), suggesting that ITG turbulence could be locally suppressed, consistent with ion thermal transport being close to neoclassical. These simulations do not include the influence of the parallel velocity gradient (PVG), the shear in the equilibrium toroidal flow projected along the field lines, which can drive instability a Kelvin-Helmholtz-like instability [68]. In the region of strong flow shear, the corresponding gradient $u'=(qR/r)\cdot\gamma_E=4$-5 is large, and does enhance the ITG growth rates around $\rho\approx 0.6$-0.65. However, even with this enhancement the local linear growth rates remain far below the local E×B shearing rate.

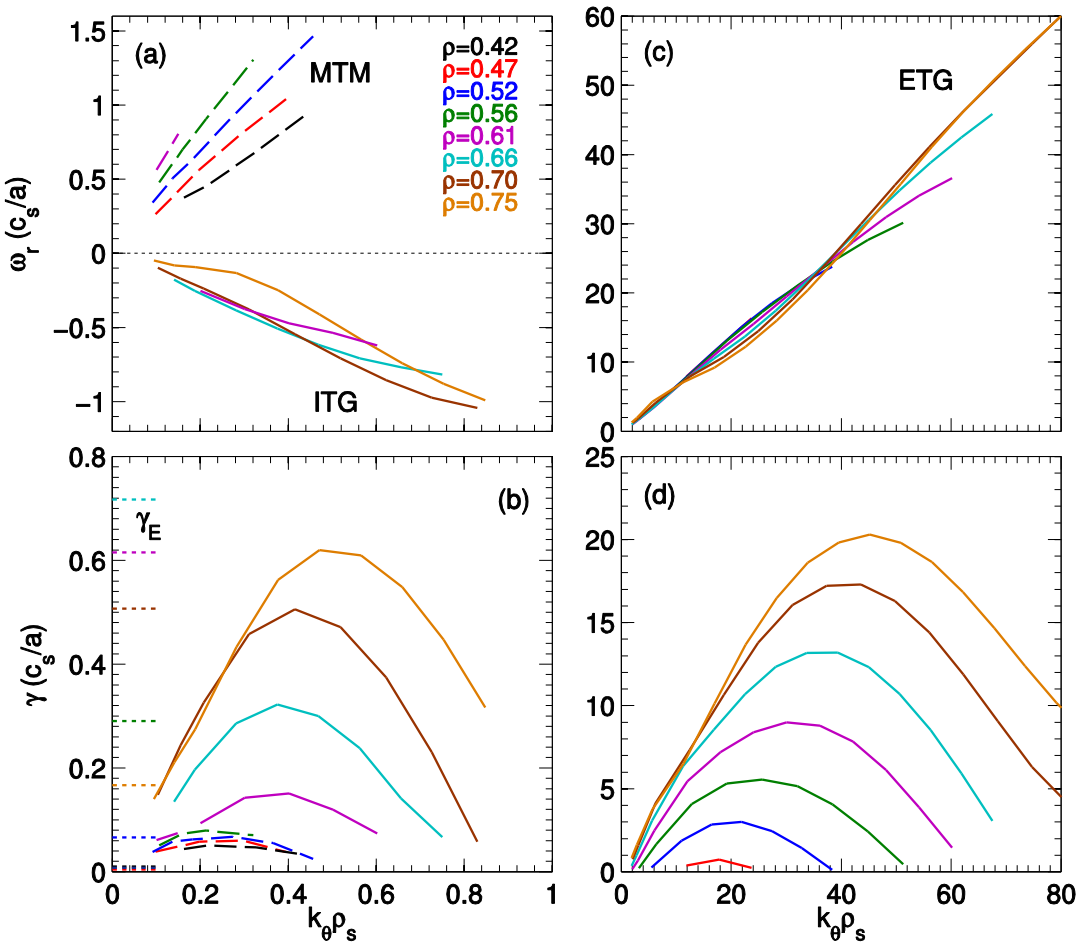

Fig. 8. (a,c) Real frequency and (b,d) linear growth rates for (left) ion scale, $k_\theta\rho_s<1$ and (right) electron scale, $k_\theta\rho_s>1$, microinstabilities. The short dashed lines in (b) show the E×B shearing rates, γ_E.

In addition to ITG there is also a spectra of unstable microtearing modes (MTMs) at ion scales in the region of ρ=0.42-0.61 (dashed lines in Fig. 9a,b), with growth rates peaking around $k_\theta\rho_s$~0.2. The MTM are distinguished from the ITG as they have tearing parity (odd-parity potential φ perturbations, even-parity shear magnetic $A_\parallel$ perturbations), strong magnetic fluctuation amplitudes $[(\delta A_\parallel/\rho_s\cdot B_0)$ / $(e\delta\varphi/T_e) \sim 1]$, and they propagate in the electron diamagnetic drift direction (positive real frequencies in Fig. 8a). Microtearing modes are fundamentally electromagnetic in nature, requiring shear magnetic perturbations $\delta B_\perp=\nabla\times\delta A_\parallel$, and are often predicted in ST H-modes at higher beta and collisionality [14,69]. The presence of unstable MTM is somewhat unexpected in the L-mode plasmas as beta was expected to be low enough to avoid the onset of MTM, a key motivation for running these discharges. (Similar ITG+MTM micro-stability characteristics were predicted recently for a MAST L-mode plasma [70].) However, in these ST L-modes plasmas, the local electron beta and electron temperature gradient are apparently sufficiently large to destabilize EM microinstabilities, which could possibly contribute to the electron thermal transport. We note that MTM is not always significantly unstable in L-mode plasmas.

Indeed, additional simulations for the L-modes 204651 and 204963 show that MTM is only unstable over a smaller region ($\rho<0.45$) with much weaker growth rates due to the lower values of beta (Table I). MTM were also not predicted to be unstable in previous NSTX L-mode analysis [16] in a discharge with much lower collisionality.

In addition to ITG and MTM at ion scales, electron scale ($k_\theta\rho_s>>1$) ETG instabilities are also unstable outside $\rho\geq0.47$ (Fig. 8c,d) with growth rates increasing in radius. ETG turbulence can contribute substantially to electron thermal transport, and in cases where the E×B shearing rate is sufficiently large to suppress ion scale turbulence, electron-scale nonlinear simulations can be used to predict the amount of transport from ETG turbulence [71-73] (discussed below). However, recent work has also shown that multi-scale simulations are required to predict the correct transport when ion scale turbulence is near-marginal or above threshold [74], as in some locations here.

Fig. 9a,b presents a summary of the linear stability results for 204551, showing the radial profile of the maximum growth rates for each instability (ITG, MTM, ETG) and the local E×B shearing rates. (Both ITG simulations with and without finite parallel velocity gradient (u') are shown in Fig. 9a). As the mode-dominance between ITG and MTM varies radially, the GYRO eigenvalue solver [75] is used to track the sub-dominant instability. Based purely on local considerations, the strong E×B shearing rate is expected to suppress transport over a substantial region where $\gamma_E>(\gamma_{ITG},\gamma_{MTM})$. Outside $\rho=0.7$ (R=140 cm) is where ITG growth rates begin to significantly surpass the E×B shearing rates, consistent with the increasing BES fluctuation amplitudes (Fig. 6c). In the region of $\rho\approx0.6$-0.7 both ITG and MTM are linearly unstable. These instabilities propagate in different directions, with phase velocities in the plasma frame (no Doppler shift) of $V_{ph,ITG,sim}$ = +(0.5-1) km/s (ion direction) and $V_{ph,MTM,sim}$ = –(2-3) km/s (electron direction). While this is qualitatively similar to the bi-modal propagation observed in the BES measurements, the measured phase velocities differ substantially. Nonlinear simulations coupled with synthetic diagnostics [76] are required to make a direct quantitative comparison between simulation and experiment and will be pursued in the future.

Additional linear simulations were performed in two other discharges (204963, 204651) at different plasma current, density and NBI power (Table I). The results for 204963 are shown in Fig.9c,d, and show qualitatively similar profiles of ITG, MTM, and ETG, although the quantitative strengths are varied. In this case, at lower injected power and torque, ITG growth rates are larger due to reduced T_i/T_e (since $R/L_{Ti,crit\text{-}ITG}\sim1+T_i/T_e$ [77,78]), while E×B shearing rates are reduced. The larger values of γ_{ITG}/γ_E suggest ITG turbulence could be more important at ion scales. An increase in measured BES fluctuation amplitudes is consistent with this simple linear stability interpretation. On the other hand, MTM growth

rates are reduced due to lower beta, while ETG growth rates are also reduced due to increased T_e/T_i (since $R/L_{Te,crit\text{-}ETG} \sim 1+Z_{eff} \cdot T_e/T_i$ [79]).

Inspecting Fig. 9, there is a substantial variation in ion scale stability and E×B shearing rate over ~20% of the minor radius. In the region ρ=0.5-0.7 this corresponds to a width of ~30 ρ_i ($\rho_* = \rho_i/a = 1/150$ at ρ=0.6). As radial correlation lengths are often ~5·ρ_i, nonlocal effects are likely to be important in determining the nonlinear nature of the ion scale turbulence. Global electrostatic nonlinear simulations [28] for an NSTX L-mode plasma [29] unstable to ITG/TEM show that non-local effects are important at similar ρ_*, as they smooth out strong radial variation in transport predicted from local simulations. Global electromagnetic nonlinear simulations will be required to verify how non-local effects influence nonlinear saturation of the ITG+MTM turbulence in the NSTX-U L-mode and whether bimodal cross-phases are expected.

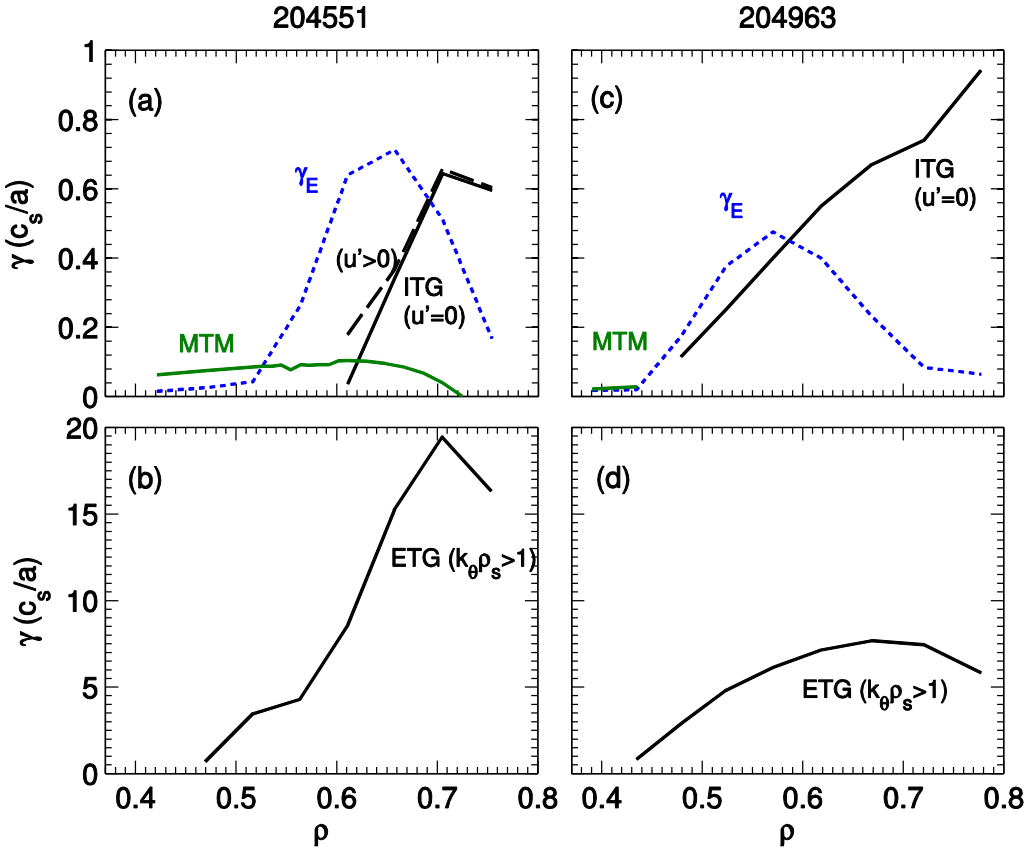

Fig. 9. Radial profile of (a,c) ITG and MTM growth rates and (b,d) ETG growth rates for shots 204551 (top) and 204963 (bottom). E×B shearing rate is shown by the dashed blue line. The simulations with finite parallel velocity gradient ($u' > 0$) are shown by the dashed black line in (a).

Nonlinear ETG simulations

In the region of ρ=0.6 the E×B shear is sufficiently strong to expect complete suppression of ion scale turbulence in the *local* limit. In this region the ETG instability has relatively large growth rates.

Under these conditions it is straightforward to run nonlinear electron scale simulations (i.e. no multi-scale effects) to predict electron heat flux contributions from ETG turbulence.

The base nonlinear ETG simulations used the following numerical grids in GYRO as determined from previous studies and convergence tests [73,80]: perpendicular box size $L_x \times L_y \approx 6 \times 4\ \rho_s$ ($360 \times 240\ \rho_e$), 48 complex toroidal modes, 192 radial grid points, 12 energies, 12 pitch angles, and 14 parallel mesh points ($\times 2$ signs of parallel velocity). Edge buffer zones at the radial boundaries ($\Delta^b = 1\ \rho_s$ wide) are used to damp n=0 perturbations in these simulations that use Dirichlet boundary conditions [66]. The effective range of non-zero wavenumbers simulated are $(k_\theta \rho_s, k_r \rho_s)_{min} \approx 1.5$, $(k_\theta \rho_s, k_r \rho_s)_{min} \approx 73$. The linear ETG threshold gradient has a well-known dependence proportional to Z_{eff}, $R/L_{Te} \sim (1 + Z_{eff} \cdot T_e/T_i)$ [79] (in the limit of weak density gradients, applicable at these radii). We expect this to influence the nonlinear results so two sets of simulations were run with different values of Z_{eff}=1.2 and 2.

Fig. 10 shows a comparison of the predicted ETG electron heat flux at four radial locations (ρ=[0.47, 0.56, 0.66, 0.75]) compared to the experimental heat flux inferred from TRANSP (using the assumption that ion thermal transport is neoclassical, as discussed in Sec. III). The predicted heat flux peaks at $\rho \sim 0.56$. Moving inwards the ETG flux decreases as ETG becomes linearly stable, while moving outwards the predicted heat flux drops as the gyroBohm factor drops, $Q_{GB,e} = (\rho_e/a)^2 n_e v_{Te} T_e \sim T_e^{5/2}$. The heat flux at this location varies between 0.7-1.7 MW, spanning the experimental value, $Q_{e,exp}$=1.2+/-0.5 MW. For reference, the heat flux of $Q_{e,ETG}$=0.7 MW corresponds to a gyroBohm-normalized electron thermal diffusivity of $\chi_e = 12 \cdot \rho_e^2 v_{Te}/L_{Te}$, similar to values predicted in other nonlinear ETG simulations [73,81].

The gyrobohm-normalized heat flux spectra (Fig. 10b) show that the peak in ETG transport is predicted to occur around $k_\theta \rho_s$=10. The contributions at smaller wavenumbers at ρ=[0.56,0.66] falls off by an order of magnitude, consistent with the strong E×B shear suppressing ion scale turbulence in this region. At ρ=0.75, the low $k_\theta \rho_s$ contributions do not fall off as significantly, due partially to increase in relative linear ETG drive. In this region the ITG growth rates are larger than E×B shearing rates. Under such conditions, recent real-mass multi-scale simulations have shown the multi-scale effects can change the total transport and relative contribution between ion and electron heat flux in non-intuitive ways. It may be necessary to consider similar multi-scale simulations to account for transport in these discharges. As non-local, finite-ρ_* effects may also be important, it may be necessary to pursue seek global, multi-scale simulations (e.g. [82]).

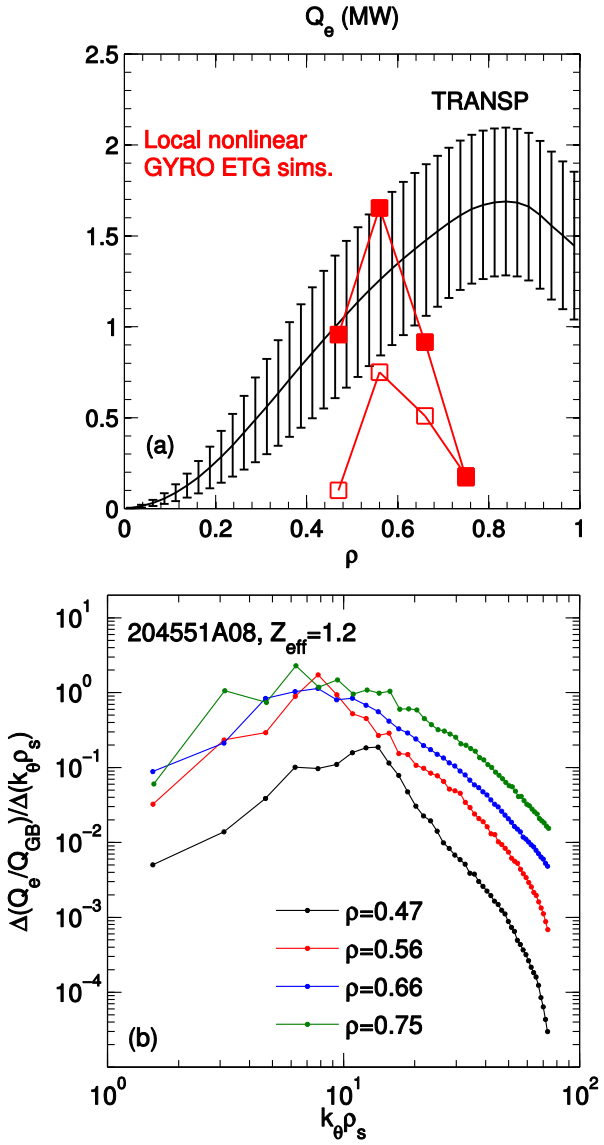

Fig. 10. (a) Predicted electron heat flux from nonlinear ETG simulations using two different values of Z_{eff} compared with experimentally inferred electron heat flux from TRANSP. (b) Normalized electron heat flux spectra simulated at four radii using Z_{eff}=1.2.

VI. Discussion and summary

A variety of stationary L-mode plasmas were successfully developed during the first run campaign of the National Spherical Torus Experiment – Upgrade (NSTX-U) project. The plasmas span a range of density (1-4×10^{19} m^{-3}), plasma current (0.65-1.0 MA), and neutral beam heating power (≤4 MW), taking advantage of new, more tangential neutral beam sources to vary rotation profiles. Normalized beta values between β_N~1-2 (R/a~1.6) were achieved for 0.5-1 second flat-top. These conditions provide an experimental "intermediate" (R/a, β_N) target that bridges high aspect ratio, low beta (R/a ~ 3, β_N ~ 1-2) where the bulk of gyrokinetic validation studies exist, and low aspect ratio, high beta

($R/a \sim 1.5$, $\beta_N \sim 5$) where GK simulations are less tested and challenged by stronger electromagnetic, equilibrium, and non-local effects (at large $\rho_* = \rho_i/a$).

Linear gyrokinetic stability analysis indicates that in these L-mode plasmas, electromagnetic, non-local and multi-scale effects may all be important. Electrostatic ITG modes are unstable at ion scales ($k_\theta \rho_i < 1$), although the E×B shearing rates can be larger than the linear growth rates over some regions ($\rho > 0.7$). This is consistent with the TRANSP analysis showing that ion thermal transport is near neoclassical predictions and that electron transport dominates thermal losses. Fluctuation amplitudes measured at ion scales from beam emission spectroscopy (BES) increase in amplitude at increasing radii, consistent with the relative increase in γ_{ITG}/γ_E, suggesting ITG turbulence may be more important further out. In the higher beta L-modes ($\beta_N \sim 2$), electromagnetic MTM are also unstable at ion scales. The BES cross-phase measurements also indicate bimodal turbulence phase velocities that propagate in electron and ion diamagnetic direction at low (<50 kHz) and high (>50 kHz) frequency, respectively. This feature may be indicative of different turbulence mechanisms (such as ITG and MTM), although analysis is ongoing to ensure this feature is not a result of common-mode beam fluctuations due to edge shadowing.

The ion scale growth rates and E×B shearing rates are predicted to vary significantly over a narrow width, ~30 ρ_i ($\rho = 0.5$-0.75) due to the relatively large values of $\rho_* = \rho_i/a \sim 1/150$ in these plasmas. Global electromagnetic nonlinear simulations will be required to verify how non-local effects influence nonlinear saturation of the ITG+MTM turbulence in the NSTX-U L-mode and whether bimodal cross-phases are expected.

Finally, electron temperature gradient (ETG) modes at smaller scales ($k_\theta \rho_i > 1$) are also predicted to be unstable. Local, nonlinear simulations of ETG turbulence predict significant electron heat flux between $\rho = 0.45$-0.65 where $\gamma_E > \gamma_{ITG}, \gamma_{MTM}$. If global simulations indicate complete E×B suppression of ion scale turbulence does not occur in the finite-ρ_* limit, these discharges may require global multiscale simulations.

Acknowledgements

We would like to thank the entire NSTX-U Team for supporting development and operations of the plasmas used in this research. W.G. would specifically like to thank R. Raman, D. Battaglia, M.D. Boyer, N.A. Crocker, D. Darrow, N. Ferraro, S.P. Gerhardt, D. Liu, J.E. Menard, C. Myers, and D. Mueller for useful discussions, as well as J. Candy for making the GYRO code available. This research utilized resources of the National Energy Research Scientific Computing Center, supported by US DOE Contract DE-AC02-05CH11231. This work was also supported by DOE contract DE-AC02-09CH11466.

References

[1] S.M. Kaye et al., Nucl. Fusion **47**, 499 (2007).

[2] S.M. Kaye et al., Phys. Rev. Lett **98**, 175002 (2007).

[3] S.M. Kaye et al., Nucl. Fusion **53**, 063005 (2013).

[4] M. Valovič et al., Nucl. Fusion **49**, 075016 (2009).

[5] M. Valovič et al., Nucl. Fusion **51**, 073045 (2011).

[6] Y.-K.M. et al., Plasma Physics Control. Fusion **47**, B263 (2005).

[7] Y.-K.M. Peng et al., Fusion Sci. Technol. **56**, 957 (2009).

[8] G.M. Voss et al., Fusion Eng. Des. **83**, 1648 (2008).

[9] M. Kotschenreuther, P. Valanju, S. Mahajan, E. Schneider, Fusion Eng. Des. **84**, 83 (2009).

[10] B. Kuteev et al., Nucl. Fusion **51**, 073013 (2011).

[11] J.E. Menard et al., Nucl. Fusion **51**, 103014 (2011).

[12] J.E. Menard et al., Nucl. Fusion **56**, 105023 (2016).

[13] W. Guttenfelder, J. Candy, S.M. Kaye, W.M. Nevins, E. Wang, R.E. Bell, G.W. Hammett, B.P. LeBlanc, D.R. Mikkelsen, H. Yuh, Phys. Rev. Lett **106**, 155004 (2011).

[14] W. Guttenfelder, J. Candy, S.M. Kaye, W.M. Nevins, R.E. Bell, G.W. Hammett, B.P. LeBlanc, H. Yuh, Phys. Plasmas **19**, 022506 (2012).

[15] W. Guttenfelder, J. Candy, S.M. Kaye, W.M. Nevins, E. Wang, J. Zhang, R.E. Bell, N.A. Crocker, G.W. Hammett, B.P. LeBlanc, D.R. Mikkelsen, Y. Ren, H. Yuh, Phys. Plasmas **19**, 056119 (2012).

[16] W. Guttenfelder, J.L. Peterson, J. Candy, S.M. Kaye, Y. Ren, R.E. Bell, G.W. Hammett, B.P. LeBlanc, D.R. Mikkelsen, W.M. Nevins, H. Yuh, Nucl. Fusion **53**, 093022 (2013).

[17] H. Doerk, F. Jenko, M.J. Pueschel and D.R. Hatch, Phys. Rev. Lett. **102**, 155003 (2011).

[18] M.J. Pueschel, M. Kammerer and F. Jenko, Phys. Plasmas **15**, 102310 (2008).

[19] M.J. Pueschel and F. Jenko, Phys. Plasmas **17**, 062307 (2010).

[20] R.E. Waltz, Phys. Plasmas **17**, 072501 (2010).

[21] M.J. Pueschel et al., Phys. Rev. Lett. **110**, 155005 (2013).

[22] A. Ishizawa, S. Maeyama, T.-H. Watanabe, H. Sugama, N. Nakajima, Nucl. Fusion **53**, 053007 (2013).

[23] A. Ishizawa, T.-H. Watanabe, H. Sugama, S. Maeyama, N. Nakajima, Phys. Plasmas **21**, 055905 (2014).

[24] H. Biglari, P.H. Diamond, P. Terry, Phys. Fluids B **2**, 1 (1990).

[25] R.E. Waltz, G.D. Kerbel, J. Milovich, Phys. Plasmas **1**, 2220 (1994).

[26] K.H. Burrell, Phys. Plasmas **4**, 5 (1997).

[27] P.W. Terry, Rev. Mod. Phys **72**, 109 (2000).

[28] W.X. Wang et al., Phys. Plasmas **22**, 102509 (2015).

[29] Y. Ren et al., Nucl. Fusion **53**, 083007 (2013).

[30] H. Doerk, F. Jenko, T. Görler, D. Told, M.J. Pueschel, D.R. Hatch, Phys. Plasmas **19**, 055907 (2012).

[31] A.K. Swamy, R. Ganesh, J. Chowdhury, S. Brunner, J. Vaclavik, L. Villard, Phys. Plasmas **21**, 082513 (2014).

[32] I. Holod, Z. Lin, Phys. Plasmas **20**, 032309 (2013).

[33] T. Görler et al., Phys. Plasmas **23**, 072503 (2016).

[34] C. Holland et al., Nucl. Fusion **52**, 063028 (2012).

[35] J. Abiteboul, T. Görler, F. Jenko, D. Told, and the ASDEX Upgrade Team, Phys. Plasmas **22**, 092314 (2015).

[36] A. Bañón-Navarro, D. Told, F. Jenko, T. Görler, Tim Happel and the ASDEX Upgrade Team, Phys. Plasmas **23**, 042312 (2016).

[37] W. Wan et al., Phys. Rev. Lett. **109**, 185004 (2012).

[38] W. Wan et al., Phys. Plasmas **20**, 055902 (2013).

[39] D.R. Smith et al., Nucl. Fusion **53**, 113029 (2013).

[40] I. Holod, D. Fulton, Z. Lin, Nucl. Fusion **55**, 093020 (2015).

[41] D.R. Hatch et al., Nucl. Fusion **56**, 104003 (2016).

[42] J.E. Menard, S. Gerhardt, M. Bell et al., Nucl. Fusion **52**, 083015 (2012).

[43] S.P. Gerhardt, R. Andre, J.E. Menard, Nucl. Fusion **52**, 083020 (2012).

[44] J.E. Menard, IAEA-FEC OV/5-2, Kyoto, Japan (2016); submitted to Nucl. Fusion "Overview of the first operational and physics results from NSTX Upgrade".

[45] L.L. Lao, H. St. John, R.D. Stambaugh, W. Pfeiffer, Nucl. Fusion **25**, 1421 (1985).

[46] S.A. Sabbagh, S.M. Kaye, J. Menard et al., Nucl. Fusion, **41**, 1601 (2001).

[47] S.P. Gerhardt, D.A. Gates, S.M. Kaye et al., Nucl. Fusion **51**, 073031 (2011).

[48] B.P. LeBlanc, R.E. Bell, D.W. Johnson, D.E. Hoffman, D.C. Long, R.W. Palladino, Rev. Sci. Instrum. **74**, 1659 (2003).

[49] R.E. Bell and R. Feder, Rev. Sci. Instrum. **81**, 10D724 (2010).

[50] R.J. Hawryluk, *An empirical approach to tokamak transport*, Physics of Plasmas Close to Thermonuclear Conditions ed B. Coppi et al (Brussels: CEC) vol. 1, pp 19-46 http://w3.pppl.gov/transp/papers/Hawryluk.pdf

[51] A. Pankin, D. McCune, R. Andre, G. Batemann, A. Kritz, Computer Phys. Comm. **159**, 157 (2004).

[52] C.S. Change, F.L. Hinton, Phys. Fluids **25**, 1493 (1982).

[53] W.A. Houlberg, K.C. Shaing, S.P. Hirshman, M.C. Zarnstorff, Phys. Plasmas **4**, 3230 (1997).

[54] E.A. Belli, J. Candy, Plasma Phys. Control. Fusion **50**, 095010 (2008).

[55] E.A. Belli, J. Candy, Plasma Phys. Control. Fusion **54**, 015015 (2012).

[56] S.M. Kaye et al., Nucl. Fusion **37**, 1303 (1997).

[57] D.R. Smith, H. Feder, R. Feder, et al., Rev. Sci. Instrum **81**, 10D717 (2010).

[58] N. Schoenbeck et al., Rev. Sci. Instrum **81**, 10D718 (2010).

[59] D.R. Smith, R.J. Fonck, G.R. Mckee, D.S. Thompson, Rev. Sci. Instrum **83**, 10D502 (2012).

[60] G.R. McKee, P. Gohil, D.J. Schlossberg et al., Nucl. Fusion **49**, 115016 (2009).

[61] Z. Yan, P. Gohil, G.R. McKee et al., IAEA-FEC EX/5-1, Kyoto, Japan (2016).

[62] Y-C. Ghim, A.R. Field, D. Dunai, S. Zoletnik, L. Bardoczi, A.A. Schekochihin and the MAST Team, Plasma Phys. Control. Fusion **54**, 095012 (2012).

[63] R.D. Durst, R.J. Fonck, G. Cosby, H. Evensen, S.F. Paul, Rev. Sci. Instrum **63**, 4907 (1992).

[64] J. Candy and R.E. Waltz, Phys. Rev. Lett. **91**, 045001 (2003).

[65] J. Candy and R.E. Waltz, J. Comput. Phys. **186**, 545 (2003).

[66] J. Candy and E. Belli, General Atomics Technical Report No. GA-A26818 (2010).

[67] J. Candy, Plasma Phys. Control. Fusion **51**, 105009 (2009).

[68] P.J. Catto, M.N. Rosenbluth, C.S. Liu, Phys. Fluids **16**, 1719 (1973).

[69] D.J. Applegate, C.M. Roach, J.W. Connor, S.C. Cowley, W. Dorland, R.J. Hastie, N. Joiner, Plasma Phys. Control. Fusion **49**, 1113 (2007).

[70] W. Guttenfelder, A.R. Field, I. Lupelli, T. Tala, S.M. Kaye, Y. Ren, W.M. Solomon, IAEA-FEC TH/P3-14 Kyoto, Japan (2016); submitted to Nucl. Fusion (in review).

[71] J. Candy, R.E. Waltz, M.R. Fahey, C. Holland, Plasma Phys. Control. Fusion **49**, 1209 (2007).

[72] C.M. Roach, I.G. Abel, R.J. Akers, W. Arter, M. Barnes, Y. Camenen, F.J. Casson, G. Colyer, J.W. Connor, S.C. Cowley, D. Dickinson, W. Dorland, A.R. Field, W. Guttenfelder, G.W. Hammett, R.J. Hastie, E. Highcok, N.F. Loureiro, A.G. Peeters, M. Reshko, S. Saarelma, A.A. Schekochihin, M. Valovic, H.R. Wilson, Plasma Phys. Control. Fusion **51**, 124020 (2009).

[73] W. Guttenfelder, J. Candy, Phys. Plasmas **18**, 022506 (2011).

[74] N. Howard, C. Holland, A.E. White, M. Greenwald, J. Candy, Nucl. Fusion **56**, 014004 (2016).

[75] E.A. Belli and J. Candy, Phys. Plasmas **17**, 112314 (2010).

[76] C. Holland, NF 2009 (synth, diag)

[77] F. Romanelli, Phys. Fluids B **1**, 1018 (1989).

[78] T.S. Hahm, W.M. Tang, Phys. Fluids B **1**, 1185 (1989).

[79] F. Jenko, W. Dorland, G.W. Hammett, Phys. Plasmas **8**, 4096 (2001).

[80] Y. Ren, W. Guttenfelder, S.M. Kaye et al., Phys. Plasmas **19**, 056125 (2012).

[81] W.M. Nevins, J. Candy, S. Cowley et al., Phys. Plasmas **13**, 122306 (2006).

[82] F. Jenko, D. Told, T. Görler, J. Citrin, A. Bañón Navarro, C. Bourdelle, S. Brunner, G. Conway, T. Dannert, H. Doerk, D.R. Hatch, J.W. Haverkort, J. Hobirk, G.M.D. Hogewiej, P. Mantica, M.J. Pueschel, O. Sauter, L. Villard, E. Wolfrum and the ASDEX Upgrade Team, Nucl. Fusion **53**, 073003 (2013).

PPPL PRINCETON PLASMA PHYSICS LABORATORY

Princeton Plasma Physics Laboratory
Office of Reports and Publications

Managed by
Princeton University

under contract with the
U.S. Department of Energy
(DE-AC02-09CH11466)

P.O. Box 451, Princeton, NJ 08543
Phone: 609-243-2245
Fax: 609-243-2751

E-mail: publications@pppl.gov

Website: http://www.pppl.gov